Behavior factor estimation for seismic design of unreinforced masonry buildings

Noura Zarzour, Maria Paola Santisi D'avila, E. Diego Mercerat, Luca Lenti, Michel Oggero

Case Studies in Construction Materials 19 (2023) e02483

Contents lists available at ScienceDirect

Case Studies in Construction Materials

journal homepage: www.elsevier.com/locate/cscm

Behavior factor estimation for seismic design of unreinforced masonry buildings

Noura Zarzour [a,c,*], Maria Paola Santisi d'Avila [a], E. Diego Mercerat [b], Luca Lenti [b], Michel Oggero [c]

[a] Université Côte d'Azur, Polytech'Lab, UPR, 7498, Biot, France
[b] CEREMA, Repsody, Sophia Antipolis, France
[c] FILIATER, Nice, France

ARTICLE INFO

Keywords:
Ductility
Behavior factor
Pushover analysis
Geo-sourced construction material
Unreinforced masonry building
Equivalent frame approach

ABSTRACT

The use of new geo-sourced construction materials in seismic areas requires the assessment of the structure ductility in order to properly design the building. This research aims to propose a procedure for behavior factor estimation in case of using a new construction material. In particular, in this paper, the proposed methodology is applied to an unreinforced masonry building in an average-risk seismic zone. Before application for seismic design, the reliability of the selected equivalent frame modeling approach is validated by comparison of dynamic features obtained from both numerical and operational modal analysis. An existing stone masonry building is selected as case study to validate the modeling approach. A measurement campaign provides the structural response to ambient vibrations and structural damping. After validating the model in elastic conditions, the building ductility capacity is estimated using a numerical pushover analysis, for different load combinations and distributions, according to the European design code, under the assumption of perfect plasticity. The proposed procedure provides a behavior factor obtained specifically for the analyzed building, using a relationship between ductility demand and behavior factor deduced from dynamic analysis. The average ductility demand is estimated numerically, for a set of synthetic acceleration signals compatible with the Eurocode elastic response spectrum and a given behavior factor. Finally, it is suggested to verify the near collapse limit state of the building structure not only in terms of target to capacity displacement ratio but also in terms of load ratio, since it can be more restrictive in some instances.

1. Introduction

The transition towards a circular economy by 2050 encourages the use of geo-sourced construction materials that are more respectful of the planet. However, the use of new building materials is still limited by the difficulty of properly assessing the structural performance, especially in seismic areas, where the behavior under dynamic loading and the structural ductility have to be considered. This makes it difficult to obtain technical certification and insurance for new construction in seismic zones. The lack of specific studies on building ductility would lead the designers to use the maximum seismic demand proposed by design codes, for safety. In particular,

* Correspondence to: Université Côte d'Azur, Polytech'Lab, UPR 7498, 930, Route des Colles, 06410 Biot, France.
E-mail address: noura.zarzour@etu.univ-cotedazur.fr (N. Zarzour).

https://doi.org/10.1016/j.cscm.2023.e02483
Received 2 June 2023; Received in revised form 8 September 2023; Accepted 17 September 2023
Available online 18 September 2023

the interest in geo-sourced masonry constructions increases, justified not only by its low environmental impact but also by the desire to keep the memory of local constructive typologies for the integration in the landscape and the tourism attractiveness of the territories.

The mechanical behavior of masonry can be investigated using different approaches [34], depending on the balance between accuracy level and both modeling and computation time: a detailed micro-modeling approach considering unit and mortar separately in the spatial discretization and, consequently, distinct constitutive relationships for each material and their interface [1,2,49]; a simplified micro-modeling approach considering expanded units and defining the constitutive relationships for unit and interface, already including the mortar [33,35,51]; and the macro-modeling approach [26,37,46,48,50], in which a constitutive relationship is used for masonry, intended as a homogenized material. The macro-modeling approach is often associated with the equivalent frame modeling strategy [32,38,50] for masonry buildings.

In this research, the seismic performance of unreinforced masonry (URM) buildings is investigated by adopting the equivalent frame approach, in which the building is represented by deformable elements (piers and spandrels), connected by rigid nodes. This modeling technique is suggested for earthquake design in the current version of the Eurocode 8 (EC8, [18]) and is considered as a reasonable compromise between precision of results and modeling and computational effort, in the case of engineering practice. According to Galasco et al. [25], an equivalent beam element having bilinear elasto-perfectly plastic (EPP) behavior is adopted to model piers and spandrels. This beam element model is able to couple the response to shear, flexure and axial force according to strength domains for the masonry panels and to represent the main in-plane masonry failure modes, such as bending-rocking and shear mechanisms. The equivalent frame approach is applied to an existing stone masonry house, selected as case study. It is built in Levens (South of France) which is an average-risk seismic zone according to the French seismic hazard zonation map. A measurement campaign of its structural response, under ambient vibration, is undertaken using velocity sensors. The dynamic properties of the building are obtained by inversion of velocity time histories, in terms of natural frequencies and mode shapes, using operational modal analysis tools [6,7]. The selected model validation approach consists in comparing the dynamic features of the building, obtained by both numerical and operational modal analysis [7,10,17,21,24,27,40]. This allows the validation of the equivalent frame model, under the hypothesis of global box-like behavior (guaranteed by chaining of walls and good connection between each slab and walls), as well as of the assumption of orthotropic diaphragm for wood slabs.

According to European design provisions [18], the building stability verification can be performed by comparing displacement capacity and demand, in the framework of a pushover analysis [31] in which a quasi-static horizontal load is applied at each floor, assigned according to a selected distribution along the building height, and the constitutive behavior of construction materials is assumed as elasto-plastic. Otherwise, the building stability verification can be performed by equivalent lateral force or response spectrum analyses, in which the seismic demand is reduced by a behavior factor, if some ductility is expected for the analyzed building, in the case of plastic deformation.

Uang [55] expresses the behavior factor $q = q_0\ OSR$ as the product of the force reduction factor q_0 and the overstrength ratio OSR. The force reduction factor q_0 accounts for the structure capacity to dissipate hysteretic energy, while the overstrength ratio, discussed by Blume [5], is the maximum to yield strength ratio (named as α_u/α_1 in the EC8) and results from the internal force redistribution. A causal relationship exists between q_0 and the structure ductility μ. Miranda and Bertero [39] provide an overview of analytical $(\mu,\ q_0)$ relationships.

The investigations conducted by Veletsos and Newmark [58], and, later on, by Newmark and Hall [43,44], propose to reduce the elastic spectrum as a function of the fundamental period and ductility of the structure. Based on elastic and inelastic response spectra to the North-South component of the 6.9 M_w 18 May 1940 El Centro earthquake, they notice that elastic and inelastic single-degree-of-freedom (SDOF) systems having medium to long periods tend to reach similar displacement $u_{\max}$ at the top. According to this iso-displacement criterion, as shown in Fig. 1b, it is $(f_e - f_y)/(u_{\max} - u_y) = f_e/u_{\max}$, where $u_{\max}$ is the SDOF system displacement attained during the seismic event, u_y and f_y are the yield displacement and base shear, respectively, and f_e is the

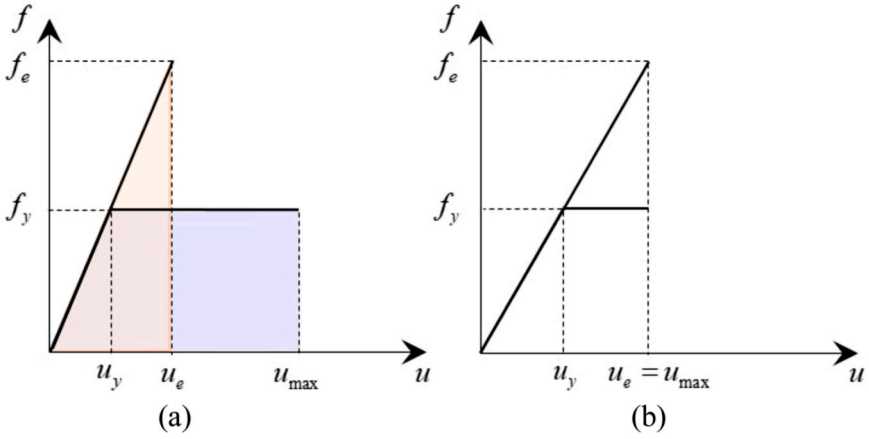

Fig. 1. (a) Principle of iso-energy for a single-degree-of-freedom system having a medium to short natural period. (b) Principle of iso-displacement for a system having a medium to long natural period.

maximum base shear ideally attained in case of linear-elastic response. As a consequence, considering the ductility demand $\mu = u_{max}/u_y$ and the strength reduction factor $q_0 = f_e/f_y$, it is $q_0 = \mu$. Moreover, for SDOF systems having a medium to short natural period, the principle of energy conservation can be used to estimate the inelastic displacement of an EPP system from the elastic displacement ideally attained in linear-elastic conditions for the same excitation. According to this iso-energy criterion, as shown in Fig. 1a, the equivalence of area under the curves is $u_e f_e/2 = f_y u_y/2 + f_y(u_{max} - u_y)$, where u_e is the system displacement in the case of linear-elastic response. Consequently, the relation $q_0 = \sqrt{2(\mu - 1)}$ is obtained.

Nassar and Krawinkler [42] study the seismic response of SDOF systems having nonlinear behavior using recorded input motions. A relationship between the force reduction factor q_0 and the ductility demand μ is proposed, including the dependence on the structure fundamental period and inelastic features.

Vidiç et al. [59] analyze the response of SDOF systems having nonlinear behavior using earthquake records and propose to estimate the force reduction factor q_0 as a function of the ductility demand, fundamental period of the SDOF system and predominant period of the ground motion, distinguishing SDOF systems having short and long period. The transitional period between these two conditions depends on the predominant period of the ground motion and the ductility. A simplification of this formulation is proposed by Fajfar [22] and then refined in the N2 method [23]. Accordingly, the transitional period is assumed equal to T_C, which is the period between the constant acceleration and constant velocity part of the response spectrum used in building codes.

Guerrini et al. [28] compare the ductility demand estimated using the N2 method and a nonlinear dynamic analysis, for a set of SDOF systems. They propose an alternative formulation relating the force reduction factor q_0 and ductility demand because they consider that the N2 method could underestimate the ductility demand, particularly for a short fundamental period of the structure.

In this research, a procedure for the estimation of the behavior factor is proposed, considering the force reduction factor related to the building ductility, evaluated using the three-dimensional (3D) model of the building. The case study discussed in this paper is an existing stone masonry building to allow the validation of the structural model, but the proposed procedure to estimate the behavior factor can be applied to any new construction material for the seismic design of buildings. The ductility capacity μ_0 of the building, defined as the ultimate to yield displacement ratio, is estimated through a pushover analysis [31]. Forty-eight pushover analyses are carried out using the 3D model of the building, considering positive and negative load for both horizontal directions, three accidental eccentricity levels and four possible load distributions. According to the proposed procedure, a ductility demand versus force reduction factor curve is also obtained using a numerical approach, specifically for the analyzed building and load combination, considering the structure dynamic features and hysteretic behavior. An average ductility demand is obtained for a set of synthetic seismic signals, generated by satisfying the compatibility criteria of the EC8 [18] with the target elastic acceleration spectrum [8]. On the other side, it is proposed to assess the seismic global stability of the building, for the near collapse limit state, not only in terms of building top displacement, as required by the EC8 [18], but also in terms of base shear force.

In Section 2, the proposed procedure for behavior factor estimation is presented. The case study is described in Section 3 and the adopted numerical model for URM buildings is validated. The results of the analysis are discussed in Section 4 and the conclusions are developed in Section 5.

2. Behavior factor estimation

The behavior factor, used in the EC8 design response spectrum formulation [18], depends on the plastic behavior of construction materials and it is related to the building ductility. The higher is the behavior factor, the lower is the seismic demand for building design. The steps of the proposed numerical procedure adopted to estimate the behavior factor of a building is described in the following subsections.

2.1. 3D model for unreinforced masonry buildings

In this research, a 3D macro-element model is adopted for URM buildings, using the equivalent frame approach, under the hypothesis of global box-like behavior, guaranteed by chaining of walls and good connection between each slab and walls. The building model is developed in 3Muri software by S.T.A. DATA, selected because it can be used in professional practice. Assuming that the out-of-plane response (local mechanism) is prevented, the in-plane behavior of each structural element, as piers and spandrels, is modeled using a 2-node Timoshenko beam having three degrees of freedom per node (two translations and a rotation in the plan). The EPP behavior is adopted as the constitutive relationship for the deformable wall panels. According to D'Altri et al. [14], in new constructions, the masonry element fails predominantly for bending-rocking, shear sliding or diagonal shear cracking of bricks [36], depending on the dimensional ratio and mortar properties. The ultimate strength criteria for piers and spandrels, related to these possible failure mechanisms are presented in Annex A1.

In URM building modeling, the roof and slabs govern the transfer of both vertical and horizontal loadings among the walls [32]. Moreover, the connection between walls and the horizontal diaphragm, as well as the choice of mechanical parameters for the orthotropic diaphragm strongly influence the building natural frequencies.

In this study, the roof and slabs are composed of joists and timber planks. The roof is considered a non-structural element. Whereas, the slabs are considered as structural elements. Vertical loads are transferred as in a one-way slab, according to joist direction, and horizontal loads are transferred considering an orthotropic diaphragm. The elastic moduli in shear and compression of the diaphragm are defined taking into account the degree of connection between walls and horizontal diaphragm [32] and, consequently, they influence the amount of horizontal force transferred among the walls. In the analyzed case study, beams are clamped into the masonry

wall and the main joists are sufficiently connected to beams. The joists in the secondary orthotropy direction and planking ensure a non-negligible shear and axial stiffness in the secondary direction. Accordingly, the elastic modulus in compression of the slab, in the main orthotropy direction, is estimated as $(E_w A_j)/(i\, t_{eff}) + E_w$, where E_w is the elastic modulus in compression of wood, A_j is the joist cross-sectional area, i is the joist spacing and t_{eff} is the effective thickness of the diaphragm. The elastic modulus in compression in the secondary orthotropy direction and the shear modulus are assumed equal to the elastic moduli of wood E_w and G_w, respectively. The flexural behavior of the slab is neglected, compared with the global building response.

2.2. Pushover analysis

A pushover analysis is carried out, using the 3D building model, by imposing a quasi-static horizontal load, incremented until the building collapse. The horizontal load is determined according to a selected distribution along the building height. In this research, the uniform and modal load distributions are considered, according to the EC8 [18]. The modal distribution is proportional to the dynamic response in the elastic regime, while the uniform one is proportional to a constant horizontal acceleration profile with height, associated with a plastic phase (also named mass-proportional distribution). Three different modal distributions are adopted, such as the triangular, unimodal and multimodal load distribution. The triangular distribution is also named height-proportional distribution because the fundamental mode shape is height-proportional in the case of floors having all the same mass. The unimodal distribution is used considering the dynamic structural response as mainly governed by the fundamental mode shape. Instead, a multimodal distribution is proportional to the structure deformation obtained by combining the modes that involve a cumulative effective mass higher than 90 % of the total mass of the building.

The pushover curve of the 3D building is obtained by relating the base shear force (reaction to the applied horizontal load at the building base) to the horizontal displacement of a selected control node at the top of the building. In this research, the average top floor displacement, weighted on the basis of nodal mass [25], is used. The pushover analysis is repeated by applying the horizontal load in the two orthogonal directions $(\pm x,\ \pm y)$ and considering an eventual accidental mass eccentricity in each direction $(0,\ \pm 5\%)$. In summary, 12 analyses are performed for 4 load distributions (48 analyses in total).

The pushover curve $(F,\ U)$ is truncated at the ultimate displacement U_u, defined as the minimum between the displacement corresponding to the failure of the first pier element and the displacement at which a 20% reduction in strength occurs after reaching the peak strength. The collapse of the pier [25] is assumed when the drift exceeds the threshold of 0.4 % in shear and 0.8 % in bending, according to the EC8 [20].

The obtained pushover curve depends on the selection of two parameters controlling the convergence: the tolerance accepted in equilibrium verification during the nonlinear analysis and the expected maximum displacement for the control node of the structure during the pushover analysis. In order to balance accuracy and convergence, the tolerance is generally selected lower than 1 %. In exceptional cases of convergence problems, it can be increased to obtain coherent results for the set of load combinations. The maximum displacement of the control node is selected close to the last displacement reached in the pushover analysis and adjusted iteratively, to have an adequate number of load increments in the analyzed displacement range.

2.3. Equivalent SDOF system and capacity curve

The pushover curves $(F,\ U)$ obtained using the 3D building model are scaled to obtain a capacity curve $(f,\ u)$ for an equivalent SDOF system. This operation, adopted in the present work, reduces the computational cost of the numerical procedure proposed for the behavior factor estimation, but it is not imperative if the same procedure is undertaken using the 3D building model.

The incremental dynamic equilibrium equation of the 3D building is expressed as

$$\mathbf{M}\,\Delta\ddot{\mathbf{D}}(t) + \mathbf{C}\,\Delta\dot{\mathbf{D}}(t) + \mathbf{K}(t)\,\Delta\mathbf{D}(t) = -\mathbf{M}\,\boldsymbol{\tau}\,\Delta\ddot{u}_g(t) \tag{1}$$

where $\Delta\mathbf{D}(t)$, $\Delta\dot{\mathbf{D}}(t)$ and $\Delta\ddot{\mathbf{D}}(t)$ are the displacement, velocity and acceleration increment vectors at the time instant t, respectively. $\mathbf{M}$, $\mathbf{C}$ and $\mathbf{K}$ are the mass, damping and stiffness matrices, respectively, $\boldsymbol{\tau}$ is the influence vector and $\Delta\ddot{u}_g$ is the ground acceleration increment. The coordinate transformation

$$\Delta\mathbf{D}(t) = \widetilde{\boldsymbol{\Phi}}_j\,\Delta U(t) \tag{2}$$

is imposed in Eq. (1) to obtain the incremental dynamic equilibrium equation of the equivalent SDOF system. $\widetilde{\boldsymbol{\Phi}}_j$ is the j-th mode shape vector (j −th eigenvector of $\mathbf{K}^{-1}\,\mathbf{M}$) or another convenient displacement shape and ΔU is the displacement increment at the building top. The selected displacement shape is normalized, that is, the value at the top is one. According to Eq. (2) and pre-multiplying by $\widetilde{\boldsymbol{\Phi}}_j^T$, Eq. (1) can be written as

$$\widetilde{\boldsymbol{\Phi}}_j^T\,\mathbf{M}\,\widetilde{\boldsymbol{\Phi}}_j\,\Delta\ddot{U}(t) + \widetilde{\boldsymbol{\Phi}}_j^T\,\mathbf{C}\,\widetilde{\boldsymbol{\Phi}}_j\,\Delta\dot{U}(t) + \widetilde{\boldsymbol{\Phi}}_j^T\,\mathbf{K}\,\widetilde{\boldsymbol{\Phi}}_j\,\Delta U(t) = -\widetilde{\boldsymbol{\Phi}}_j^T\,\mathbf{M}\,\boldsymbol{\tau}\,\Delta\ddot{u}_g(t) \tag{3}$$

The use in Eq. (3) of a shape vector $\boldsymbol{\Phi}_j$ orthonormalized with respect to the mass matrix, such as $\boldsymbol{\Phi}_j^T\,\mathbf{M}\,\boldsymbol{\Phi}_j = 1$, yields

$$\Delta\ddot{U}(t) + 2\,\zeta\,\omega_0\,\Delta\dot{U}(t) + k(t)\,\Delta U(t) = -\Gamma\,\Delta\ddot{u}_g(t) \tag{4}$$

where $\mathbf{\Phi}_j^T \mathbf{C} \mathbf{\Phi}_j = 2\,\zeta\,\omega_0$, $\mathbf{\Phi}_j^T \mathbf{K} \mathbf{\Phi}_j = k$ and the modal participation factor Γ is

$$\Gamma = \mathbf{\Phi}_j^T \mathbf{M}\,\boldsymbol{\tau} \tag{5}$$

The stiffness (normalized with respect to mass) is $k = \omega_0^2$ in elastic conditions, ω_0 is the angular frequency of the equivalent SDOF system and ζ is the damping ratio. Interested readers can refer to Chopra [12] for more details.

Considering the displacement $u(t)$ and base shear force $f(t)$ of the equivalent SDOF system as

$$u(t) = U(t)/\,\Gamma \quad f(t) = F(t)/\,\Gamma \tag{6a,b}$$

where $U(t)$ and $F(t) = -\,\Gamma\,\ddot{u}_g(t)$ are the top displacement and base shear force in the building, respectively, Eq. (4) is then expressed as

$$\Delta\ddot{u}(t) + 2\,\zeta\,\omega_0\,\Delta\dot{u}(t) + k(t)\,\Delta u(t) = -\Delta\ddot{u}_g(t) \tag{7}$$

According to Fajfar [23], the mass of the equivalent SDOF system, deduced in quasi-static conditions, is

$$m_0 = \widetilde{\mathbf{\Phi}}_j^T \mathbf{M}\,\boldsymbol{\tau} \tag{8}$$

In this research, Γ and m_0 are estimated using a vector $\widetilde{\mathbf{\Phi}}_j$ whose terms are the building horizontal displacement corresponding to a triangular distribution.

The capacity curve $(f,\ u)$, obtained as a normalized pushover curve $(F,\ U)$, according to Eq. (6), is idealized as bilinear [53]. The equivalent initial stiffness is estimated as the secant stiffness at $f = 0.7\,f_{\max}$, where $f_{\max}$ is the maximum base shear in the capacity curve. The yield force f_y is obtained according to an equivalent energy criterion (Fig. 2) by obtaining an equivalent area under the capacity curve and its bilinear idealization. The base shear value f_y is not associated with the yielding of a structural element but is obtained numerically from the capacity curve. The overstrength ratio OSR [41] is estimated as the ratio

$$OSR = f_y/f_{y1} \tag{9}$$

between the yield force f_y, in the idealized EPP curve, and the yield force f_{y1} attained in the nonlinear capacity curve when the first structural element cracks, indicated in Fig. 2 with a thick point.

According to the EPP capacity curve, the fundamental period T_0 of the equivalent SDOF system is

$$T_0 = 2\pi\,\sqrt{m_0/k} = 2\pi\,\sqrt{m_0\,u_y/f_y} \tag{10}$$

where the equivalent mass m_0 is defined in Eq. (8) and $k = f_y/u_y$. In each loading case, this period is much more representative than the fundamental period resulting from the modal analysis.

An equivalent SDOF system, characterized by the fundamental period T_0 (Eq. (10)), is defined from each one of the pushover curves obtained for each adopted load distribution and the twelve load combinations.

The ductility capacity, which represents the structure ability to deform beyond the elastic limit, is defined as the ultimate to yield displacement ratio

$$\mu_0 = u_u/u_y \tag{11}$$

and it is obtained from each EPP curve (Fig. 2).

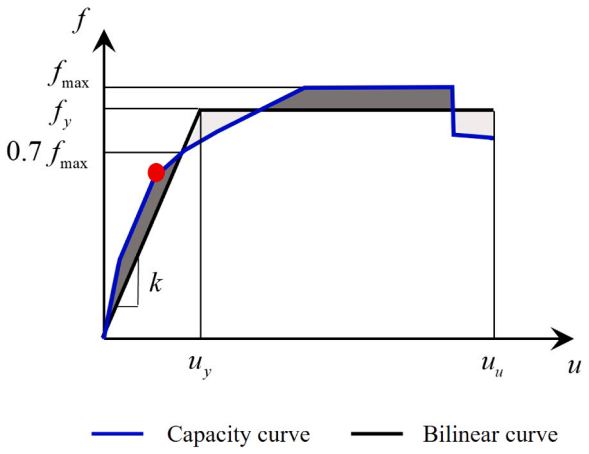

Fig. 2. Capacity curve and the associated idealized elasto-perfectly plastic curve. The first significant yield, used to determine the overstrength ratio is indicated with the thick point.

2.4. Generation of spectrum compatible seismic signals

According to the EC8 [18], a ground motion can be represented by synthetic accelerograms that have to be consistent with the assigned elastic response spectrum. In other words, for a specific damping ratio, the target EC8 response spectrum [18] and the calculated response spectrum have to match. The matching criteria are defined by the EC8 [18]. There must be no value of the mean elastic response spectrum $S_e(T)$ for all generated signals lower than 90 % of the target EC8 elastic response spectrum. Moreover, the value of acceleration for the zero period $(T = 0)$ must be higher than in the target EC8 elastic response spectrum.

The synthetic accelerograms are generated on a probabilistic basis under the assumption that an earthquake is considered as a realization of a zero-mean stationary Gaussian random process, defined by a power spectral density function, as detailed in Annex A2. An amplitude modulating function [30] is adopted to obtain nonstationary signals.

One hundred synthetic accelerograms are generated using a damping ratio $\zeta = 0.05$. The number of samples is defined according to Cacciola et al. [9]. The response spectrum parameters are selected in accordance with French provisions [15] in the discussed case study (see Section 3). The comparison of the mean response spectrum for all the synthetic accelerograms with the target EC8 elastic response spectrum [18] is shown in Fig. 3. As the compatibility criteria proposed by the EC8 [18] are verified, the generated accelerograms can be used in the nonlinear dynamic analysis.

2.5. Numerical estimation of the behavior factor

Uang [55] defined the behavior factor as the force ratio

$$q = f_e / f_{y1} \tag{12}$$

where f_e is the maximum base shear for an equivalent SDOF system in the case of linear-elastic response (Fig. 1) and f_{y1} is the yield base shear, attained when the first structural element cracks. This factor can be defined as the product of the force reduction factor q_0 and overstrength ratio *OSR* as follows:

$$q = \frac{f_e}{f_y}\,\frac{f_y}{f_{y1}} = q_0\ OSR \tag{13}$$

The definition of *OSR* from the capacity curve has been described in Section 2.3. The force reduction factor q_0 is obtained from the ductility versus force reduction factor relationship $(\mu,\ q_0)$. The procedure to obtain this curve is discussed hereinafter.

First, the dynamic response time history of the equivalent SDOF system is obtained by solving the incremental dynamic equilibrium Eq. (7), written as [11].

$$\Delta\ddot{u}(t) + 2\,\zeta\,\omega_0\,\Delta\dot{u}(t) + \Delta f_i(\Delta u(t),\ \text{sign}\ \dot{u}(t)) = -\Delta\ddot{u}_g\ (t) \tag{14}$$

where $\Delta u(t), \Delta\dot{u}(t)$ and $\Delta\ddot{u}(t)$ are the lateral displacement, velocity and acceleration increment, respectively, at each time instant t. The damping ratio ζ is estimated from the recorded structure response to ambient vibration and the synthetic accelerograms $\ddot{u}_g(t)$, generated to be compatible with the EC8 elastic response spectrum (Section 2.4), are used as input motions. The internal lateral force f_i is estimated using the constitutive relationship $f_i(u,\ \text{sign}\ \dot{u})$, idealized as EPP and expressed as

$$\begin{aligned} f_i(t) &= k\,u(t) && |u| \le u_y \quad \text{or} \quad \dot{u}(t)\,\dot{u}(t-dt)\ \le 0 \\ f_i(t) &= \text{sign}\ \dot{u}(t)\,f_y && |u| > u_y \end{aligned} \tag{15}$$

Accordingly, the system is elastic with initial stiffness $k = \omega_0^2$ as long as the force does not exceed the yield force f_y, corresponding to the yield displacement u_y. In the plastic phase, for EPP behavior, the stiffness of the SDOF is zero. When unloading, the sign of velocity $(\text{sign}\ \dot{u})$ changes and the stiffness is $k = \omega_0^2$, as well as when reloading. Considering design purposes, the yield displacement of the

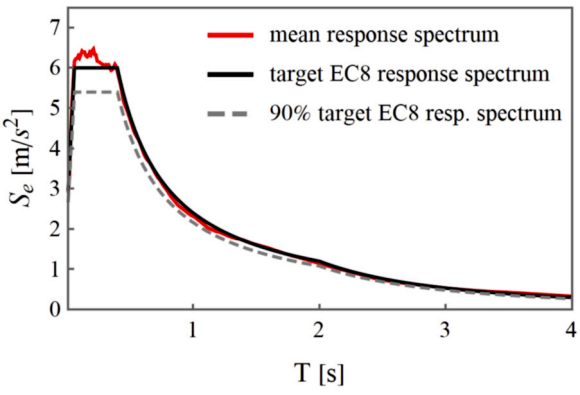

Fig. 3. Mean response spectrum for the one hundred synthetic acceleration time histories compared with the target EC8 elastic response spectrum.

equivalent SDOF system is assumed equal to the design seismic demand

$$u_y = S_a(T_0,\ q_0)\ (T_0/2\pi)^2 \tag{16}$$

where $S_a(T_0,\ q_0)$ is the EC8 design response spectrum [18] for the fundamental period T_0 of the equivalent SDOF system and the force reduction factor q_0. The step-by-step solution of the dynamic equilibrium Eq. (14) is solved according to the implicit Newmark algorithm [29], using as integration parameters $\beta = 0.3025$ and $\gamma = 0.6$, to ensure unconditional stability of time integration process. The proposed procedure for behavior factor estimation can be applied using any other numerical process for the time integration of Eq. (14). Then, the ductility demand, related to each ground motion and the selected force reduction factor q_0 (imposed in Eq. (16)), is defined as the maximum to yield displacement ratio

$$\mu = \max_t |u(t)| / u_y \tag{17}$$

The variation of the force reduction factor q_0 in a selected range $[1,\ 4]$ leads to a ductility demand versus force reduction factor relationship $(\mu,\ q_0)$, for the given fundamental period T_0 and damping ratio ζ of the equivalent SDOF system, and for each seismic motion. An average curve $(\overline{\mu},\ q_0)$ is obtained with respect to the set of generated seismic motions. The force reduction factor q_0 is estimated from the $(\overline{\mu},\ q_0)$ curve for the ductility capacity μ_0 of the equivalent SDOF system (Eq. (11)). An interpolation procedure is adopted using the log-log plot of the $(\overline{\mu},\ q_0)$ curve, as proposed by Chopra [12]. Finally, the behavior factor q is obtained by Eq. (13), related to the ductility capacity (Eq. (11)) and *OSR* (Eq. (9)), for the 48 EPP capacity curves.

In Fig. 4, the flowchart of the proposed numerical procedure is represented, adopted to determine the behavior factor q of a building, in case of using a new construction material, when the expected ductility is unknown: (1) from the 3D model of the building, (2) estimate pushover curves $(F,\ U)$ for the analyzed load combinations; (3) determine the capacity curves $(f,\ u)$ of the equivalent SDOF system, having EPP behavior, fundamental period T_0, ductility capacity μ_0 and overstrength ratio *OSR*, for each load combination; (4) from the EC8 elastic response spectrum $S_e(T)$, (5) generate a set of n synthetic accelerograms; (6) for the seismic demand $S_a(T_0,\ q_0)$, in a range of force reduction factor q_0, (7) calculate the dynamic response of the equivalent SDOF system; (8) the average $(\overline{\mu},\ q_0)$ curve is obtained with respect to the set of generated seismic motions and the force reduction factor q_0 is estimated from the $(\overline{\mu},\ q_0)$ curve for the ductility capacity μ_0 of each equivalent SDOF system; finally, the behavior factor q is obtained.

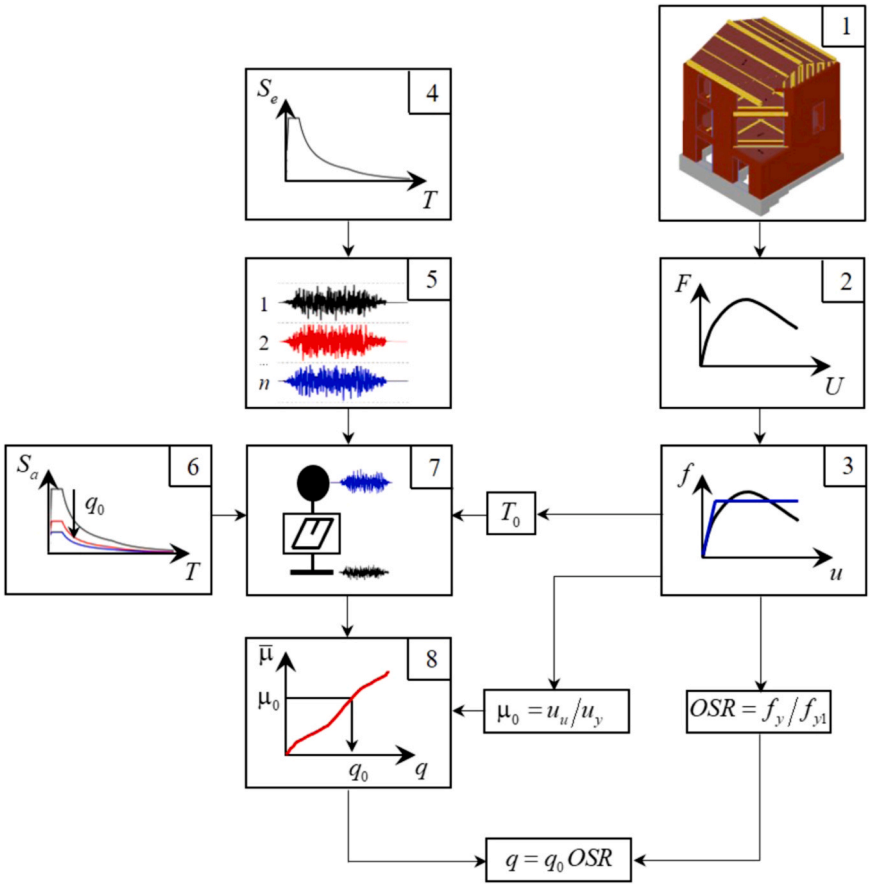

Fig. 4. Flowchart of the proposed numerical procedure to determine the behavior factor.

2.6. Verification of global stability of the building

According to the European building design code [20], at the near collapse limit state, the target displacement U_t [18], associated with the seismic demand, has not to exceed the ultimate top displacement of the building U_u, at the selected control point. This means that the system capacity must be higher than the seismic demand given by the response spectrum. It represents a safety criterion in terms of ductility. The target displacement u_t for the equivalent SDOF system is estimated as

$$\begin{array}{llll} u_t = u_e & T_0 \geq T_C & & \\ u_t = u_e & T_0 < T_C & \text{and} & f_y/m \geq S_e(T_0) \\ u_t = u_e/q_u(1 + (q_u - 1)\, T_C/T_0) \geq u_e & T_0 < T_C & \text{and} & f_y/m < S_e(T_0) \end{array} \tag{18}$$

where

$$u_e = S_e(T_0)(T_0/(2\,\pi))^2 \tag{19}$$

and $S_e(T_0)$ is the elastic acceleration response spectrum for the fundamental period T_0 of the equivalent SDOF system. According to Fajfar [23], the limit period T_C is used to distinguish short and medium to long periods of the system. The target displacement of the building U_t is evaluated as

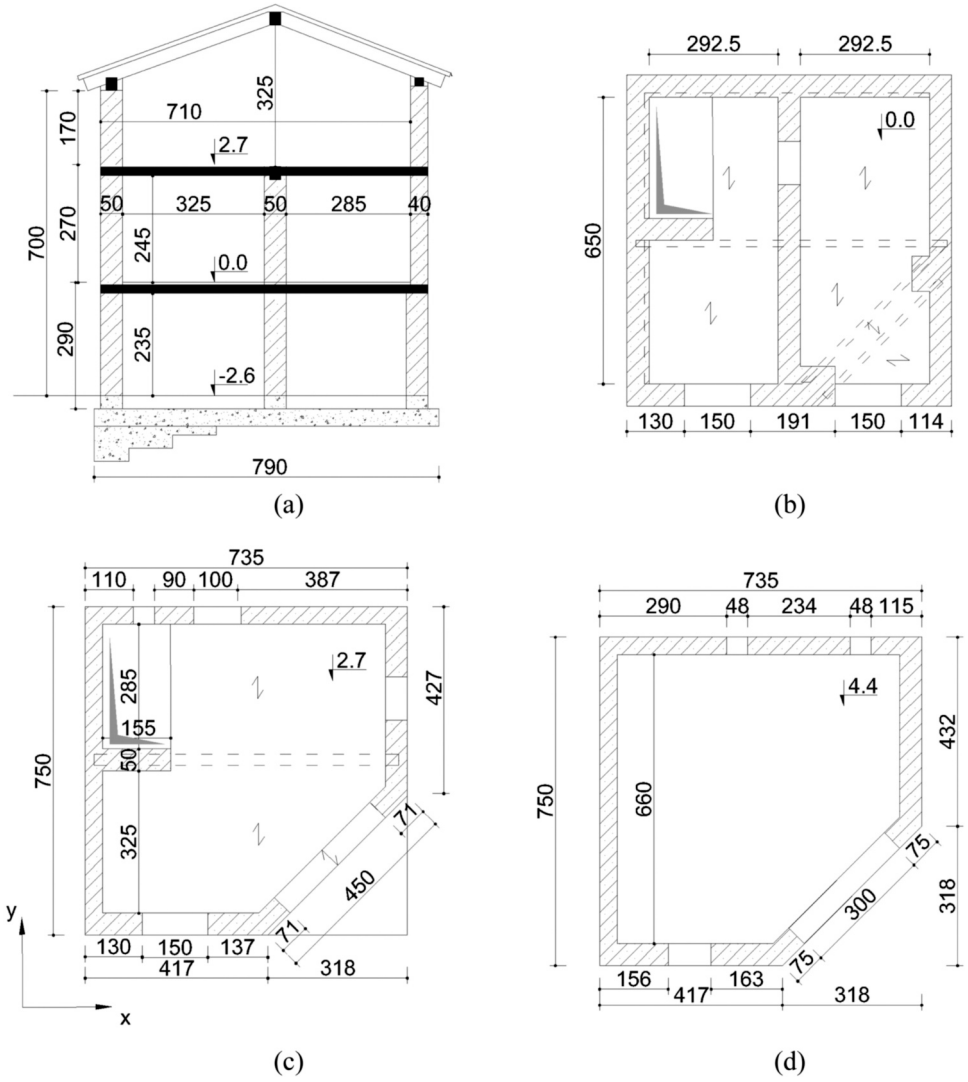

Fig. 5. Vertical section (a) and horizontal section of first (b), second (c) and third (d) level of a 3-floor stone masonry building. The dimensions are in centimeters.

$$U_t = \Gamma\, u_t \tag{20}$$

where Γ is the participation factor defined in Eq. (5). According to the EC8 [18], the load ratio

$$q_u = m_0\, S_e(T_0)/f_y \tag{21}$$

represents the target load of an SDOF system with unlimited elastic behavior, normalized with respect to the yield force f_y of an SDOF system with elasto-plastic behavior.

Moreover, in this research, it is proposed also a safety criterion related to the base shear force, inspired by the Italian code [45] in which a limit of 4 is given for the load ratio q_u in the near collapse limit state. It must be verified that the force reduction factor q_0 estimated for the building, in each load condition, is higher than the load ratio q_u (Eq. (21)).

3. Case study

A 3-floor masonry building is selected as case study. The construction plans are shown in Fig. 5. The bearing structure consists of stone masonry walls with earth mortar (Fig. 6a). The roof and slabs are composed of joists and timber planks (Fig. 6b). The walls are connected by tie rods (Fig. 6c) on each floor. This prevents out-of-plane failures and ensures a global box-like behavior of the building under seismic loading.

The building is constructed in an average-risk seismic zone (named 4 in the French seismic hazard zonation map). The foundation ground type is classified as C and the building importance class is two (II), according to the EC8 [18].

3.1. Natural frequencies of the building

An ambient vibration recording campaign is carried out to validate the 3D numerical model of the building. Guralp CMG40T velocity sensors are placed inside and outside the building. Six sensors are used for each set-up, connected to a CityShark digitizer to have synchronized velocity time histories. A sampling frequency of 200 Hz is used.

The first three natural frequencies and mode shapes of the building are identified by operational modal analysis using the Frequency Domain Decomposition technique [6,7]. The first singular values of the cross power spectral density matrix are displayed in Fig. 7. The natural frequencies, defined by peak picking, are $f_1 = 7.4$ Hz, $f_2 = 9.7$ Hz and $f_3 = 14.5$ Hz. The low-strain structural damping is estimated by the random decrement technique [13]. Values between 1.5 and 2 % are estimated for the first three modes. Considering that the façades are composed of stone walls, the damping is associated only with the structural behavior. The damping ratio $\zeta = 1.5$ % is adopted in the following computations.

3.2. Equivalent 3D frame model

The equivalent 3D frame model of the masonry building is represented in Fig. 8, in which piers, spandrels and rigid connections between them are distinguished. The foundation is modeled as a fixed connection, even if it is graphically represented in Fig. 8.a. The mechanical parameters of construction materials are summarized in Table 1. Mechanical parameters of wood (Table 1) are defined according to the C18 strength class. The slab is modeled as an orthotropic membrane, as explained in Section 2.1. Considering that the building is uninhabited, the dead load corresponding to the non-structural elements is estimated equal to 10 $\mathrm{kg/m^2}$ for the first and second floor (Fig. 5a) and 70 $\mathrm{kg/m^2}$ for the roof. Compression tests on triplet masonry specimens provide the average compressive strength f_m (Table 1).

The 3D macro-element model is validated taking advantage of the ambient vibration recording campaign. Considering that the building is uninhabited, the uncertainty is more related to the Young modulus of masonry (stiffness) than to the live load as it is not present.

The Young modulus E of masonry is calibrated to match the fundamental frequency obtained by the operational modal analysis, obtaining a value (indicated in Table 1) very close to that observed during the compression tests on triplet masonry specimens. It is

(a) (b) (c)

Fig. 6. (a) The texture of stone masonry wall, (b) timber beams, joists and plank of floor slab and (c) tie rods connections between walls.

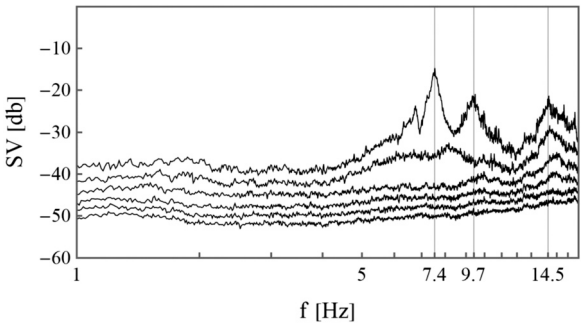

Fig. 7. Singular value (SV) spectra and identification of the first three building natural frequencies indicated by the vertical lines.

assumed a shear modulus $G = 0.4\,E$ (Table 1), according to Eurocode 6 [19].

According to the Eurocode 6 [19], the friction coefficient $\tan\varphi$ is assumed equal to 0.4 and the limit value of the tensile strength in shear is estimated as $f_{v,\,\mathrm{lim}} = 4.9$ MPa. The shear strength of masonry in pure shear, obtained by linear regression of the results of an inclined shear couplet test on two stone blocs separated by mortar, is $f_{v0} = 0.26$ MPa. In the case of irregular masonry (Fig. 6a), the shear tests on couplets could overestimate the shear strength and a better estimation would be obtained by pushover tests of wall specimens. The assumption of the drift limits proposed by the EC8 [20] is considered consistent with the analyzed stone masonry.

As stated in Section 2.1, the connection between walls and the horizontal diaphragm, as well as the choice of mechanical parameters for the orthotropic diaphragm, strongly influence the natural frequencies. Moreover, natural frequencies are impacted by the imposed position of the slab with respect to the beams, because the equivalent frame idealization is modified based on it. In particular, in this study, the second natural frequency is better reproduced considering the correct slab position, 10 cm above the beam centroidal axis.

After calibrating the model, matching the first three natural frequencies (Table 2), the first three mode shapes are validated by comparison of results obtained by operational and numerical modal analysis (Fig. 9). The modal assurance criterion MAC [47] is adopted to compare experimental and numerical translational mode shapes (Table 2). The effective mass associated with each mode shape, estimated by the numerical modal analysis, is also given in Table 2. The first and second mode shapes correspond to a translation in the *x*- and *y*-direction (see the coordinate system in Fig. 5), respectively, while the third one is a torsion. The first two natural frequencies are well reproduced (Table 2). The error of 22% in the third natural frequency is justified by the limits of the model that does not take into account the rotation of walls with respect to the vertical axis.

3.3. Loading conditions and distributions

After validation of the model, a live load has been added (200 $\mathrm{kg/m^2}$ on each floor and 170 $\mathrm{kg/m^2}$ on the roof) in the framework of building design. The seismic load combination given in EC8 [18] considers the sum of the dead load G and each live load Q multiplied by both coefficients φ and ψ_2. The adopted coefficient φ, depending on the floor occupancy, is $\varphi = 0.5$ for the floor and $\varphi = 1$ for the roof. The coefficient ψ_2, depending on the building intended use, is $\psi_2 = 0.3$ for residential areas.

In this case study, the first translational mode shape is quite a dominant mode (effective mass of 69.6 %, as indicated in Table 2). Consequently, the unimodal load distribution in *x*-direction can be considered accurate. The multimodal distribution is obtained considering 14 mode shapes in *x*-direction and 21 mode shapes in *y*-direction to attain a cumulative effective mass of 90 %.

4. Results and discussion

In this section, the results obtained for the 4 load distributions (uniform, triangular, unimodal, and multimodal) and the 12 load combinations are presented and discussed.

4.1. Capacity curves

According to Augenti and Parisi [3], the capacity curves obtained using a uniform load distribution attain higher base shear forces, compared with the unimodal and triangular distributions. This is because the centroid of loading distribution is located at a lower height ($H/2$ instead of $2/3\,H$ for a triangular distribution) inducing a reduced tilting moment. The results obtained using a multimodal distribution and a dynamic analysis are intermediate.

The capacity curves for loading directions $\pm x$ and $\pm y$ (see the coordinate system in Fig. 5) are presented in Fig. 10, in the case of uniform, multimodal, triangular and unimodal load distribution. The thick point in each capacity curve of Fig. 10 indicates the first significant yield and the associated base shear f_{y1} is used to estimate the *OSR* (Eq. (9)).

As expected, similar results are obtained for the three accidental eccentricity levels $(0,\ \pm 5\%)$ and, consequently, the impact of eccentricity on the overall resistance of this building is not significant. On the contrary, the loading direction influences the strength of the building. The strength difference related to load direction $(\pm)$ can be explained by the fact that axial load changes (mainly in piers

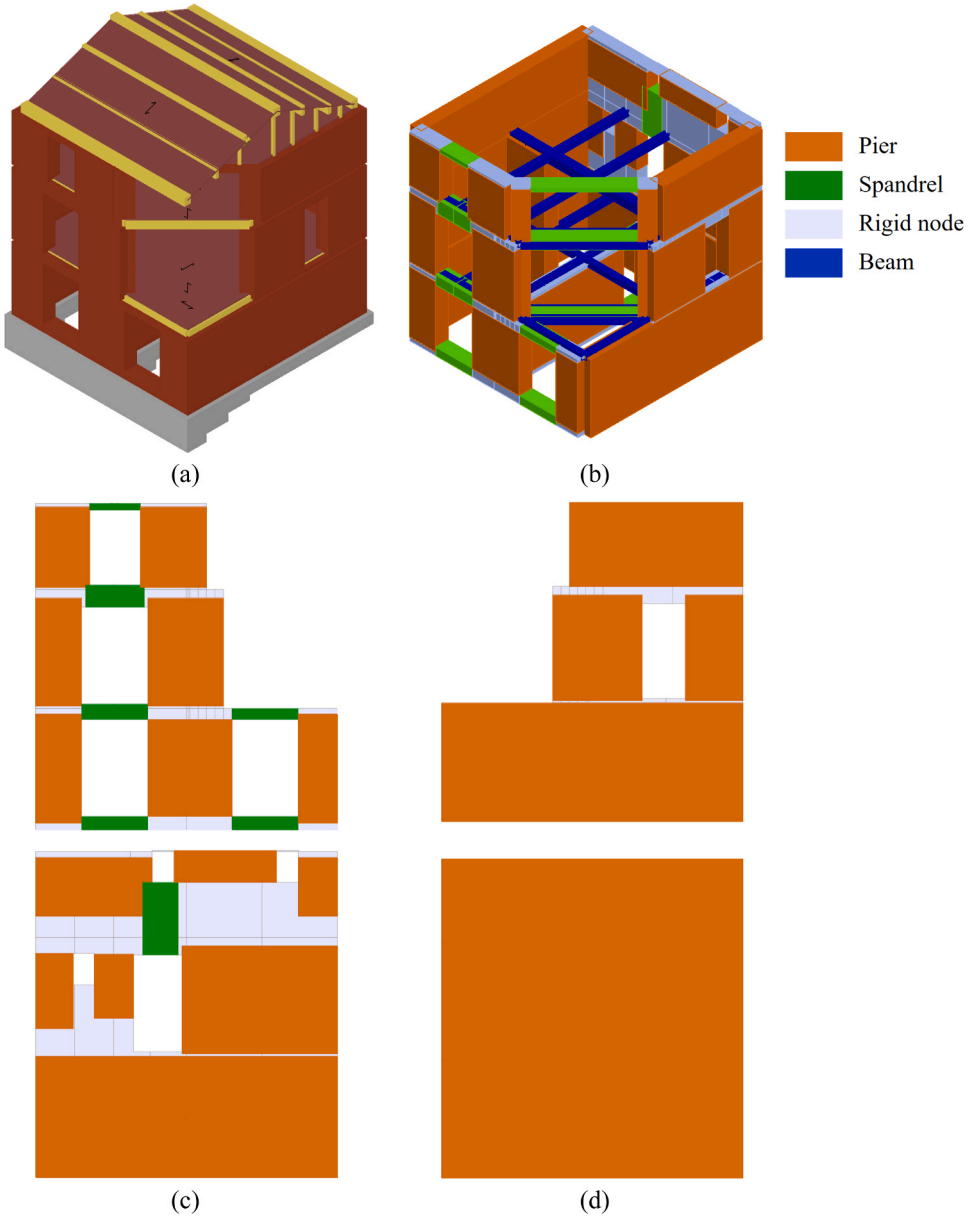

Fig. 8. (a) 3D model of the building; (b) 3D equivalent frame model, distinguishing piers, spandrels and beams; equivalent frames of façades in *x*-direction (c) and *y*-direction (d).

Table 1
Mechanical parameters of the construction materials.

		Stone masonry	Wood
Mass density	ρ (kg/m^3)	2500	400
Young modulus	E (MPa)	3750	9000
Shear modulus	G (MPa)	1500	560
Average strength in compression	f_m (MPa)	22.7	26.0
Shear strength in pure shear	f_{v0} (MPa)	0.26	
Friction coefficient	tan φ	0.4	
Tensile strength in shear	$f_{v,lim}$ (MPa)	4.9	

Table 2
Dynamic features obtained by numerical (NMA) and operational (OMA) modal analysis: natural frequencies, modal assurance criterion (MAC), effective mass.

	Mode 1	Mode 2	Mode 3
NMA: frequency (Hz)	7.3	9.9	11.2
OMA: frequency (Hz)	7.4	9.7	14.5
Error (%)	1	2	22
MAC (%)	92.6	67.9	-
Effective mass in *x*-direction (%)	69.6	0.05	0.9
Effective mass in *y*-direction (%)	0.0	31.3	0.4

close to the edges of the frame) with the variation of the load direction, leading to a variation in the dominant failure mode occurring in the panel [32]. Moreover, the building strength in the *y*-direction (Fig. 10b) is much higher than in the *x*-direction (Fig. 10a), due to the presence of much more wall length in *y*-direction and openings in *x*-direction (Fig. 5). The unimodal and uniform distribution yields the lowest and highest strength (Fig. 10), respectively, as discussed by Augenti and Parisi [3], as well as the lowest and highest elastic stiffness. This is easier to observe in Fig. 11 in which the EPP curves associated with the capacity curves are displayed distinguishing the load distribution, for each load direction.

All the parameters deduced from the 48 EPP capacity curves, such as the fundamental period T_0 of the equivalent SDOF system (Eq. (10)), its mass m_0 (Eq. (8)), participation factor Γ (Eq. (5)), yield base shear f_y (Fig. 2), ductility capacity μ_0 (Eq. (11)) and overstrength ratio *OSR* (Eq. (9)) are listed in Annex A3 (Tables A1-A4).

4.2. Ductility versus force reduction factor

The average $(\overline{\mu},\ q_0)$ curve with respect to the set of one hundred ground motions is obtained for the 48 analyses and displayed in Fig. 12a. The curves associated with *x*- and *y*-direction (see the coordinate system in Fig. 5) are plotted with solid and dashed lines, respectively.

The ductility demand decreases with increasing fundamental period, for a fixed force reduction factor q_0 [28]. Considering that the natural period of the equivalent SDOF systems deduced for the two load directions *x* and *y* is quite different, the 48 curves are naturally separated into two distinguished groups. The natural period of the second mode shape $(0.1\ \mathrm{s})$, related to a translation in *y*-direction, is shorter than the fundamental period $(0.13\ \mathrm{s})$ associated with the translation in *x*-direction, consequently, for loading in *y*-direction, the average ductility $\overline{\mu}$ is higher for a fixed q_0 and the slope of $(\overline{\mu},\ q_0)$ curves is higher. The $(\overline{\mu},\ q_0)$ curve corresponding to the minimum behavior factor q for each load distribution is shown in Fig. 12b.

4.3. Behavior factor

The force reduction factor q_0 is deduced from the $(\overline{\mu},\ q_0)$ curve for the ductility capacity μ_0 (Eq. (11)) and then multiplied by the *OSR* (Eq. (9)), to obtain the behavior factor q. The results obtained for the 48 analyses are listed in Annex A3 (Tables A1-A4). The minimum behavior factor for each load distribution is listed in Table 3. The lowest behavior factors are obtained for the multimodal load distribution in *x*-direction and uniform distribution in *y*-direction. The values in Table 3 (obtained under the assumption of guaranteed box-like behavior) are consistent with those discussed by Benedetti [4] who concluded, after analyzing shaking table experimental tests performed between 1982 and 1998, that the behavior factor for URM is at least $2.5\ -\ 3$, when a box-like behavior is guaranteed.

The $(\overline{\mu},\ q_0)$ curves in Fig. 12b are compared with analytical relationships proposed in the literature, for loading in the *x*- (Fig. 13a) and *y*- (Fig. 13b) direction. The equivalent energy and displacement approach (Veletsos 1960), represented in Fig. 1, yields higher force reduction factors, as already discussed by Nassar and Krawinkler [42] and Tomaževič et al. [54]. Nassar and Krawinkler [42] and Guerrini et al. [28] seem to underestimate the force reduction factor for higher ductilities, compared with the results obtained in this study, in which the dynamic analyses are performed using nonstationary amplitude modulated synthetic signals. The curve proposed by Vidiç et al. [59] and then simplified by Fajfar [23] is the closest to the obtained numerical curves. All these analytical curves proposed in the literature are more generic and they do not consider specific features such as the damping ratio of the structure and the dynamic response.

4.4. Global stability verification

It is verified that the target displacement U_t (Eq. (20)) does not exceed the ultimate displacement U_u in the 48 analyses (see Tables 4–7) to assess the building global capacity at the near collapse limit state. Moreover, the force reduction factor q_0 is compared to the load ratio q_u (Eq. (21)).

In the *x*-direction, where the building has much lower strength, some limit values of U_t/U_u are attained for multimodal distribution ($-x$ and $-x-e$ in Table 5) and unimodal distribution ($-x$ and $-x \pm e$ in Table 6). In these same cases, q_u is slightly higher than the force reduction factor q_0 obtained for the ductility capacity of the building. The verification in terms of base shear force appears more restrictive for these load combinations.

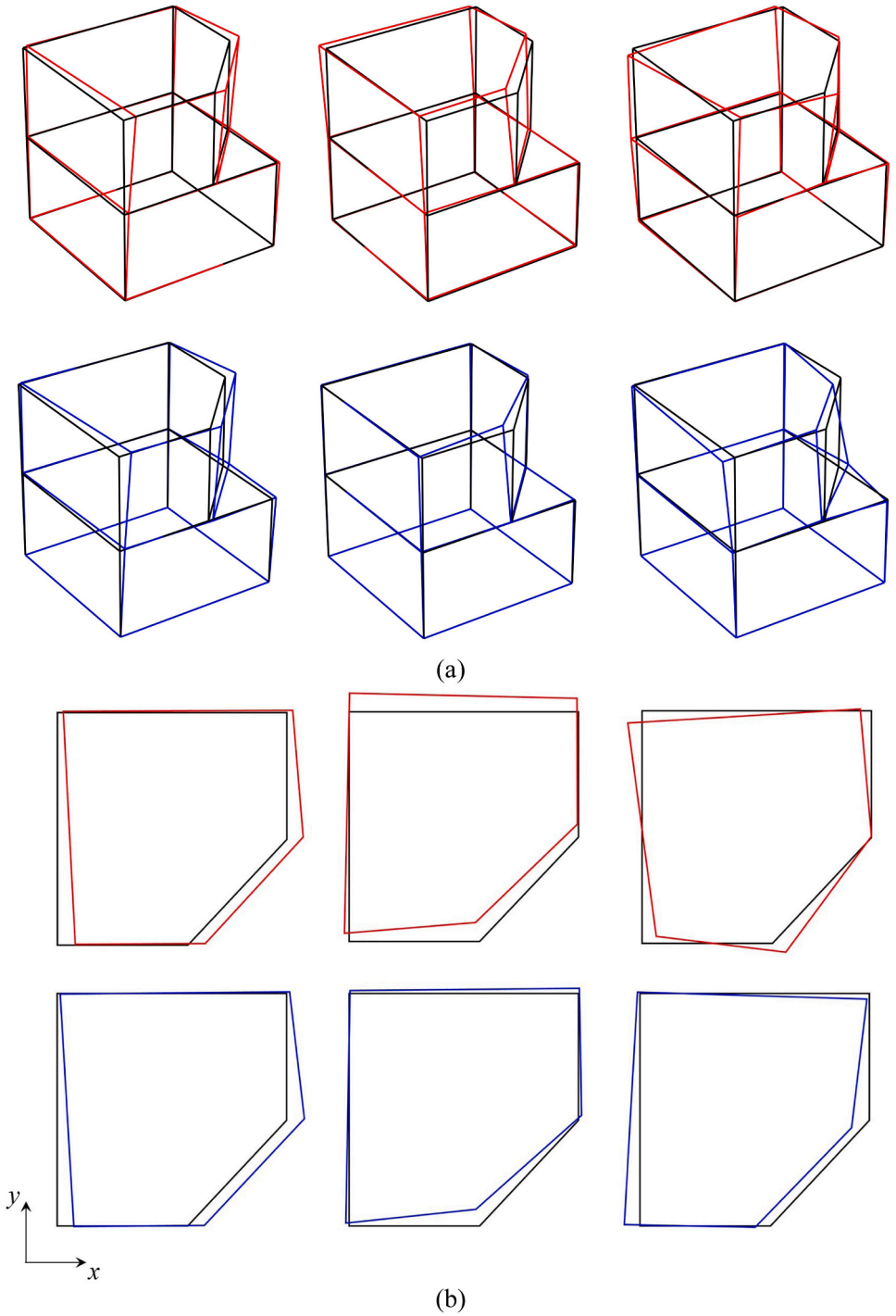

Fig. 9. Three-dimensional representation (a) and top view (b) of the first (left), second (middle) and third (right) mode shape of the analyzed stone masonry building, obtained by operational (top) and numerical (bottom) modal analysis.

5. Conclusions

This paper focuses on the behavior factor estimation for the seismic design of buildings when new construction materials are used. The increment of geo-sourced materials used in construction justifies this research, to assess the structure ductility in order to properly design the building. The proposed approach for behavior factor estimation can be adopted for any new construction material.

To begin with, this research ensures the accuracy of the selected 3D numerical model for unreinforced masonry (URM) buildings.

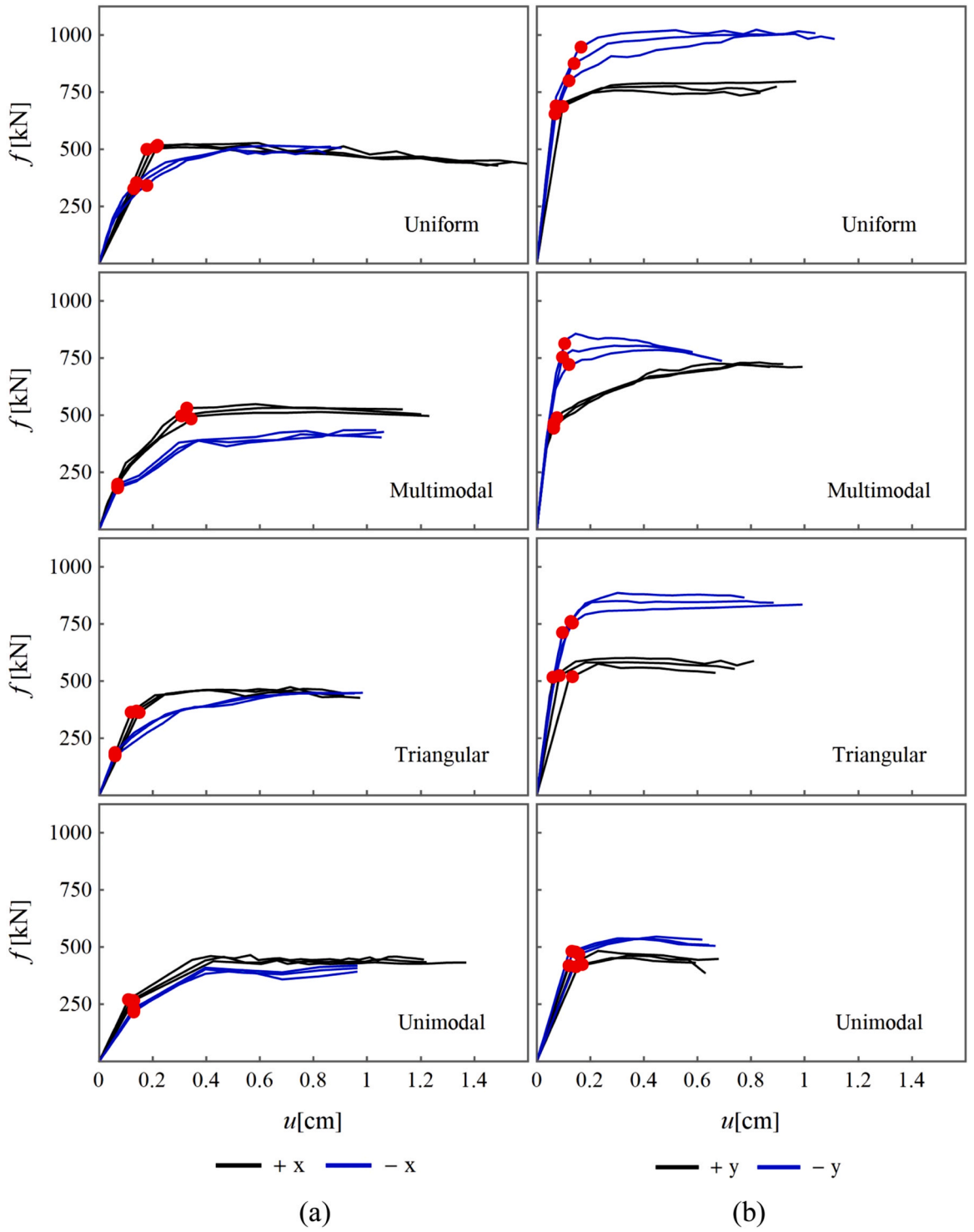

Fig. 10. Capacity curves for loading directions $\pm x$ (a) and $\pm y$ (b), in the case of four selected load distributions. The results for three accidental eccentricity levels (0, ±5%) are shown in each case. The first significant yield point is indicated in each capacity curve.

This study takes advantage of an ambient vibration recording campaign conducted in an existent three-story unreinforced stone masonry building, which is adopted as the first case study. The adopted equivalent frame model, using a macro-element approach, is validated by comparison of the dynamic features (frequencies and mode shapes) estimated by numerical and operational modal analysis.

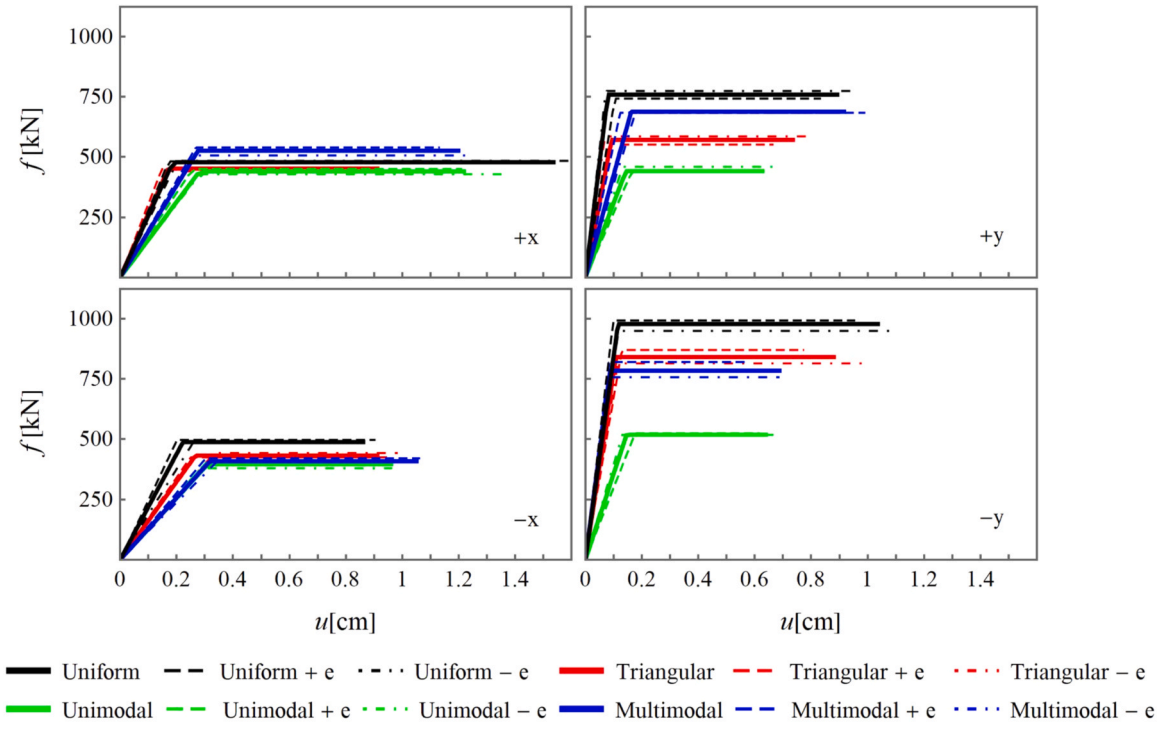

Fig. 11. Bilinear curves for 4 load distributions and 3 accidental eccentricity levels ($e = 0$, $e = \pm 5\%$) are compared for the 4 different load directions ($\pm x$, $\pm y$).

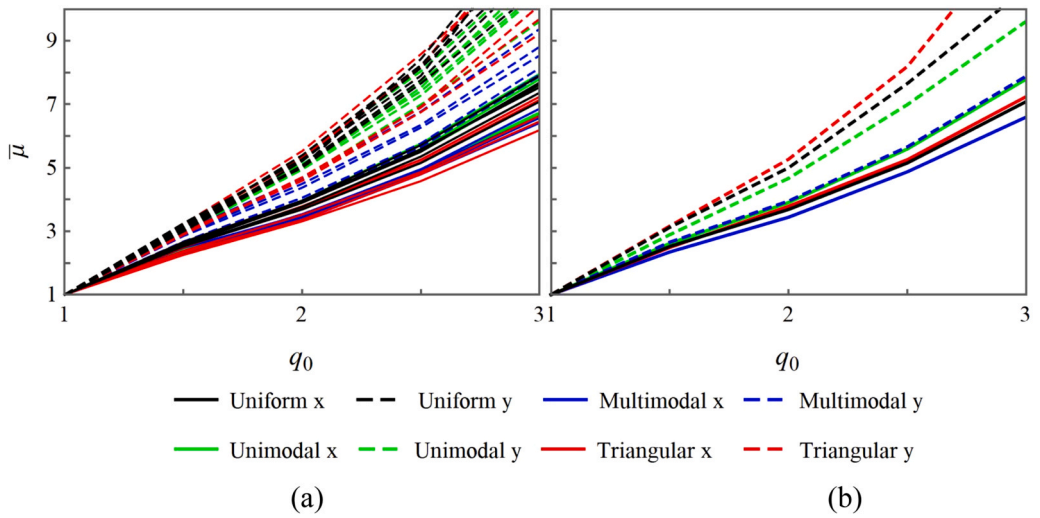

Fig. 12. Ductility versus force reduction factor curves for the analyzed stone masonry building: (a) for 4 different directions ($\pm x$, $\pm y$), 4 load distributions and 3 accidental eccentricity levels(0, $\pm 5\%$) and (b) those associated with the minimum behavior factor.

The proposed numerical procedure guarantees an estimation of the behavior factor, used to reduce the seismic demand for equivalent lateral force or response spectrum analyses, according to the expected building ductility in the case of plastic deformation. The obtained force reduction factor and behavior factor are specific for the analyzed building since they depend on the pushover curve, obtained for a given structural layout, mechanical parameters and the strength domains of structural elements. Moreover, the analysis takes into account the dynamic response of the structure, for ground motions compatible with the response spectrum imposed by the seismic design code. The variation of the building ductility capacity with the adopted loading distribution and load combinations is considered by performing forty-eight pushover analyses, using the 3D building model. Uniform and multimodal distributions yield the minimum behavior factor.

Table 3
The force reduction factor q_0, overstrength ratio *OSR* and behavior factor q related to the analysis which gives the minimum q-factor. Four load distributions are considered in x- and y-direction.

Load distribution	Load combination	Period T_0 [s]	Yield force f_y [daN]	Ductility capacity μ_0	Over-strength ratio *OSR*	Force reduction factor q_0	Behavior factor $q = q_0\ OSR$
Uniform	- *x* - *e*	0.161	48935	3.53	1.77	1.92	3.39
Multimodal	+*x*-e	0.150	57152	3.53	1.29	1.85	**2.39**
Unimodal	+*x*+*e*	0.140	50591	4.18	1.21	2.07	2.51
Triangular	-*x*-*e*	0.172	38966	4.22	1.73	2.20	3.81
Uniform	+*y*+*e*	0.089	90743	4.30	1.48	1.83	**2.70**
Multimodal	- *y* +*e*	0.071	100505	5.39	1.49	2.07	3.08
Unimodal	- *y*+*e*	0.097	79357	3.73	1.61	1.73	2.79
Triangular	+*y*+*e*	0.099	79426	4.48	1.68	1.94	3.26

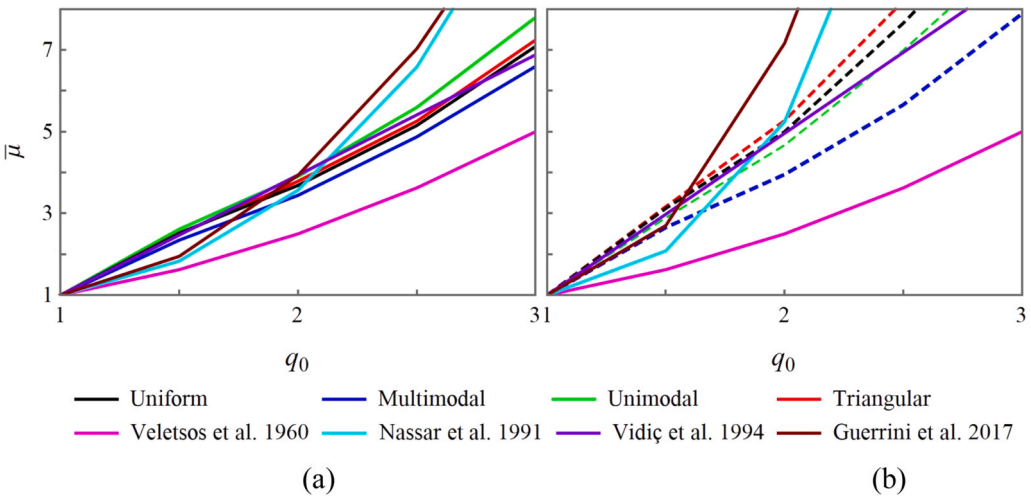

Fig. 13. Ductility versus force reduction factor curves associated with the minimum behavior factor for the analyzed stone masonry building, compared with those obtained by analytical relationships proposed in the literature, for load direction x (a) and y (b).

Table 4
Verification of the building global capacity at the near collapse limit state in the case of uniform load distribution.

Load distribution	Load combination	U_t[cm]	U_u [cm]	U_u/U_t	q_u	q_0
Uniform	+*x*	0.37	1.07	2.89	1.36	2.53
Uniform	+*x*+*e*	0.34	1.05	3.09	1.34	2.50
Uniform	+*x*-*e*	0.41	1.09	2.66	1.37	2.45
Uniform	-*x*	0.60	0.86	1.43	1.64	1.97
Uniform	-*x*+*e*	0.55	0.83	1.51	1.59	2.01
Uniform	-*x*-*e*	0.66	0.84	1.27	1.69	1.92
Uniform	+*y*	0.09	0.55	6.11	0.86	2.09
Uniform	+*y*+*e*	0.10	0.49	4.90	0.89	1.83
Uniform	+*y*-*e*	0.07	0.60	8.57	0.86	2.29
Uniform	-*y*	0.07	0.84	12.00	0.64	2.32
Uniform	-*y*+*e*	0.07	0.71	10.14	0.63	2.28
Uniform	-*y*-*e*	0.07	0.86	12.29	0.66	2.42

U_t target displacement, U_u ultimate displacement, q_u load ratio, q_0 force reduction factor.

Moreover, it is proposed to verify the near collapse limit state criteria in terms of load capacity, in the framework of a nonlinear pushover analysis, by checking that the target to capacity load ratio q_u does not exceed the force reduction factor q_0. According to Eurocode 8, the building stability verification is performed in terms of horizontal displacement at the building top. The structural stability analysis in terms of base shear force represents a complementary verification that appears more restrictive for certain load combinations.

The further step is the seismic design of a new URM building, where the masonry walls are realized using compressed earth blocks realized in situ with the earth of the construction site, using the same modeling technique. A specific experimental program is

Table 5
Verification of the building global capacity at the near collapse limit state in the case of multimodal load distribution.

Load distribution	Load combination	U_t[cm]	U_u [cm]	U_u/U_t	q_u	q_0
Multimodal	$+x$	0.50	0.93	1.86	1.39	1.96
Multimodal	$+x+e$	0.47	0.96	2.04	1.32	1.95
Multimodal	$+x$-e	0.54	0.85	1.57	1.44	1.85
Multimodal	$-x$	0.74	0.80	1.08	**1.90**	1.86
Multimodal	$-x+e$	0.78	0.88	1.13	1.84	1.90
Multimodal	$-x$-e	0.78	0.81	1.04	**1.92**	1.90
Multimodal	$+y$	0.08	0.55	6.88	0.96	2.30
Multimodal	$+y+e$	0.07	0.55	7.86	0.97	2.44
Multimodal	$+y$-e	0.09	0.55	6.11	0.96	2.30
Multimodal	$-y$	0.07	0.54	7.71	0.79	2.18
Multimodal	$-y+e$	0.07	0.43	6.14	0.79	2.07
Multimodal	$-y$-e	0.07	0.56	8.00	0.78	2.29

U_t target displacement, U_u ultimate displacement, q_u load ratio, q_0 force reduction factor.

Table 6
Verification of the building global capacity at the near collapse limit state in the case of unimodal load distribution.

Load distribution	Load combination	U_t[cm]	U_u [cm]	U_u/U_t	q_u	q_0
Unimodal	$+x$	0.55	0.79	1.44	1.63	2.02
Unimodal	$+x+e$	0.53	0.78	1.47	1.64	2.07
Unimodal	$+x$-e	0.57	0.91	1.60	1.64	2.13
Unimodal	$-x$	0.81	0.86	1.06	**2.14**	2.12
Unimodal	$-x+e$	0.82	0.85	1.04	**2.08**	2.04
Unimodal	$-x$-e	0.83	0.87	1.05	**2.18**	2.14
Unimodal	$+y$	0.41	0.47	1.15	1.64	1.74
Unimodal	$+y+e$	0.43	0.47	1.09	1.70	1.74
Unimodal	$+y$-e	0.40	0.48	1.20	1.58	1.70
Unimodal	$-y$	0.11	0.47	4.27	0.98	1.81
Unimodal	$-y+e$	0.12	0.44	3.67	1.00	1.73
Unimodal	$-y$-e	0.10	0.51	5.10	0.97	1.93

U_t target displacement, U_u ultimate displacement, q_u load ratio, q_0 force reduction factor.

Table 7
Verification of the building global capacity at the near collapse limit state in the case of triangular load distribution.

Load distribution	Load combination	U_t[cm]	U_u [cm]	U_u/U_t	q_u	q_0
Triangular	$+x$	0.48	1.11	2.31	1.57	2.62
Triangular	$+x+e$	0.45	1.26	2.80	1.56	2.89
Triangular	$+x$-e	0.51	1.03	2.02	1.56	2.38
Triangular	$-x$	0.70	1.01	1.44	2.09	2.49
Triangular	$-x+e$	0.64	0.79	1.23	2.10	2.29
Triangular	$-x$-e	0.77	0.91	1.18	2.12	2.20
Triangular	$+y$	0.15	0.56	3.73	1.08	1.99
Triangular	$+y+e$	0.12	0.55	4.58	1.01	1.94
Triangular	$+y$-e	0.13	0.61	4.69	1.06	2.21
Triangular	$-y$	0.09	0.69	7.67	0.78	2.13
Triangular	$-y+e$	0.10	0.57	5.70	0.79	1.85
Triangular	$-y$-e	0.09	0.78	8.67	0.77	2.32

U_t target displacement, U_u ultimate displacement, q_u load ratio, q_0 force reduction factor.

considered, not only to identify the mechanical and strength parameters of masonry but also the drift capacity of piers, adopted to define the ultimate displacement in the pushover analysis.

Future studies could investigate the variation of the building ductility versus force reduction factor replacing the elasto-perfectly plastic relationship of the equivalent SDOF system by a nonlinear one and directly using the dynamic response of the 3D building (pushover curve), instead of defining the equivalent SDOF system (capacity curve).

Data and Resources

This research is performed using 3Muri software by S.T.A DATA (Release 13.5.0.2). The experimental results of laboratory tests on materials, inclined shear couplet tests and compression tests on triplet masonry specimens, provided by FILIATER company, was carried by the Laboratoire de Génie Civil et Bâtiment (LGCB/LTDS) of the École Nationale des Travaux Publics de l'État (ENTPE) in Lyon (France). The ambient modal identification of the building is performed by the Repsody team of CEREMA.

Declaration of Competing Interest

The authors declare that they have no known competing financial interests or personal relationships that could have appeared to influence the work reported in this paper.

Acknowledgments

This work has been funded by the region SUD (South-Eastern France) and by FILIATER company through a doctoral fellowship. The authors thank the reviewers for the interesting remarks and discussions which improved the manuscript.

Annexes A1. Strength criteria adopted for masonry elements in the equivalent frame model

According to D'Altri et al. [14], in a new construction, the masonry element fails predominantly for bending-rocking, shear sliding or diagonal shear cracking of bricks [36], depending on the dimensional ratio and mortar properties. The ultimate strength criteria for piers and spandrels, related to these possible failure mechanisms are presented in this Annex.

The strength domains for piers are

$$\begin{aligned} M_u &= N\, l/2\, (1 - N/N_u) \\ V_u &= f_{v0}\, l'\, t + N \tan \varphi \end{aligned} \tag{22a,b}$$

According to Magenes and Della Fontana [37], the ultimate moment M_u is related to the imposed compressional force N and the maximum element capacity in compression is limited to $N_u = 0.85\, f_m\, l\, t$, where f_m is the masonry compression strength, l and t are the length and thickness of the panel, respectively. According to the Mohr-Coulomb criterion, for sliding shear in the mortar-block interface, the ultimate shear V_u is related to the imposed axial force N. The friction coefficient $\tan \varphi$ is assumed equal to 0.4 according to Eurocode 6 [19], f_{v0} is the masonry strength in pure shear and l' is the length of the compressed section of the panel. Only this shear criterion is adopted for new masonry buildings because it is considered that the sliding shear in the mortar-block interface arrives before the diagonal crack in tension induced by a shear force. A limit value of the ultimate shear $V_{u,blocks} = f_{v,\,\lim} l'\, t$ is imposed to account for the potential failure of blocks, where $f_{v,\,\lim}$ is the limit value of their tensile strength in shear. According to Eurocode 6 [19], it is adopted $f_{v,\,\lim} = 0.065\, f_b$, where f_b is the mean compressive strength of units.

The strength domains for spandrels are modified as

$$\begin{aligned} M_u &= N_p\, h/2\, \left(1 - N_p/N_{pu}\right) \\ V_u &= f_{v0}\, h\, t \end{aligned} \tag{23a,b}$$

where $N_p = 0.4\, f_m\, h\, t$, $N_{pu} = 0.85\, f_m\, h\, t$ and h is the height of the spandrel.

The collapse of the macro-element [25] is assumed when the drift exceeds the threshold of 0.4 % in shear and 0.8 % in bending [20], for both new and existing buildings.

Annexe A2. Generation of spectrum compatible seismic signals

According to Vanmarcke and Gasparini [57], a ground motion can be represented as a series of sinusoidal waves, by fixing the amplitude and generating the phase angle. In this research, a set of ground motions are generated as a superposition of n sinusoidal waves with a fixed array of amplitudes and random array of phase angles [52].

$$\ddot{u}_g(t) = \varphi(t) \sum_{i=1}^{n} \sqrt{2\, G_{\ddot{u}_g}(i\, \Delta\omega) \Delta\omega}\, \cos(i\, \Delta\omega\, t + \phi_i) \tag{24}$$

The independent random phases ϕ_i are uniformly distributed between 0 and 2 π. The amplitude modulation function $\varphi(t)$ proposed by Jennings et al. [30].

$$\varphi(t) = \begin{cases} (t/t_1)^2 & t < t_1 \\ 1 & t_1 \le t \le t_2 \\ \exp[-\beta\, (t - t_2)] & t_2 < t \le t_f \end{cases} \tag{25}$$

is adopted to preserve the stationary condition of the response process only within the strong motion phase duration T_S. It is adopted $T_s = 10$ s [18], $t_1 = 5$ s, $t_2 = t_1 + T_S$, $\beta = 0.3$ and a duration $t_f = 25$ s. The power spectral density $G_{\ddot{u}_g}(\omega)$ is selected to obtain spectrum

compatible acceleration time histories, according to Cacciola et al. [8]. The synthetic accelerograms are generated on a probabilistic basis under the assumption that an earthquake is considered a realization of a random process.

The zero-mean stationary Gaussian random process, defined by the power spectral density function, has to be consistent with the assigned elastic response spectrum. Vanmarcke and Gasparini [57] propose a relationship between the target response spectra and the power spectral density function. The prediction of the target acceleration response spectrum $S_e(\omega_i,\zeta)$, at a given angular frequency ω_i and damping ratio ζ, takes the general form

$$S_e(\omega_i,\ \zeta) = \eta_{X_i}\sigma_a \tag{26}$$

where η_{X_i} is the dimensionless peak factor of the stochastic process X_i and σ_a is the standard deviation of the dynamic response in terms of acceleration of an elastic SDOF having natural frequency ω_i and damping ratio ζ. The variance of the structural response process is [57].

$$\sigma_a^2 = G_{\ddot{u}_g}(\omega_i)\left(\frac{\pi}{4\,\zeta}-1\right)\omega_i + \int_0^{\omega_i} G_{\ddot{u}_g}(\omega)\,d\omega \tag{27}$$

According to Eqs. (26) and (27), a recursive expression of the power spectral density function compatible with the response spectrum is proposed by Vanmarck and Gasparini (1977) and modified by Cacciola et al. [8] as

$$\begin{aligned} G_{\ddot{u}_g}(\omega_i) &= 0 && 0 \le\ \omega_i \le \omega_L \\ G_{\ddot{u}_g}(\omega_i) &= \frac{4\,\zeta}{\omega_i\,\pi - 4\,\zeta\,\omega_{i-1}}\left(\frac{S_e^2(\omega_i,\zeta)}{\eta_{X_i}^2} - \Delta\omega\sum_{j=1}^{i-1} G_{\ddot{u}_g}(\omega_j)\right) && \omega_i\ > \omega_L \end{aligned} \tag{28}$$

where $S_e(\omega_i,\zeta)$ is the target acceleration response spectrum at a given angular frequency ω_i, and damping ratio ζ. The lowest bound of the existing domain of η_{X_i} is $\omega_L \cong 1$ rad/s. As proposed by Vanmarcke [56], the peak factor is evaluated as

$$\eta_{X_i} = \sqrt{2\ln\left\{2N_{X_i}\left[1-\exp\left[-\delta_{X_i}^{1.2}\sqrt{\pi\ln(2N_{X_i})}\right]\right]\right\}} \tag{29}$$

The adopted approximate evaluations of parameters in Eq. (29), provided by Der Kiureghian [16], are

$$\begin{aligned} N_{X_i} &= T_S/(2\pi)\,\omega_i\,(-\ln p)^{-1} \\ \delta_{X_i} &= \sqrt{1-[1/(1-\zeta^2)]\ \left[1-\left(2/\pi\arctan\left[\zeta\Big/\sqrt{1-\zeta^2}\right]\right)^2\right]} \end{aligned} \tag{30}$$

where T_S is the strong motion duration and p is the not-exceeding probability equal to 0.5.

Annexe A3. Detailed results

Table A1
Results obtained in the case of uniform load distribution.

Load distribution	Load combination	T_0 [s]	m_0[kg]	Γ	f_y [daN]	μ_0	OSR	q_0	q
Uniform	$+x$	0.121	137535	1.02	60813	6.37	1.76	2.53	4.45
Uniform	$+x+e$	0.118	137535	1.02	61521	6.55	1.82	2.50	4.55
Uniform	$+x$-e	0.132	137535	1.02	60611	5.52	1.71	2.45	4.19
Uniform	$-x$	0.156	137535	1.02	50642	3.72	1.90	1.97	3.74
Uniform	$-x+e$	0.146	137535	1.02	51958	3.97	1.90	2.01	3.83
Uniform	$-x$-e	0.161	137535	1.02	48935	3.53	1.77	1.92	**3.39**
Uniform	$+y$	0.084	133475	0.83	92512	5.35	1.58	2.09	3.31
Uniform	$+y+e$	0.089	133475	0.83	90743	4.30	1.48	1.83	**2.70**
Uniform	$+y$-e	0.076	133475	0.83	93249	7.13	1.72	2.29	3.94
Uniform	$-y$	0.075	133475	0.83	124856	7.54	1.51	2.32	3.50
Uniform	$-y+e$	0.073	133475	0.83	126026	6.80	1.41	2.28	3.22
Uniform	$-y$-e	0.075	133475	0.83	121048	8.12	1.56	2.42	3.78

Table A2
Results obtained in the case of multimodal load distribution.

Load distribution	Load combination	T_0 [s]	m_0[kg]	Γ	f_y [daN]	μ_0	OSR	q_0	q
Multimodal	$+x$	0.148	137535	1.02	59634	3.82	1.36	1.96	2.66
Multimodal	$+x+e$	0.146	137535	1.02	62892	3.81	1.44	1.95	2.81
Multimodal	$+x$-e	0.150	137535	1.02	57152	3.53	1.29	1.85	**2.39**
Multimodal	$-x$	0.172	137535	1.02	43536	3.32	1.32	1.86	2.45
Multimodal	$-x+e$	0.177	137535	1.02	44831	3.32	1.46	1.90	2.78
Multimodal	$-x$-e	0.174	137535	1.02	42796	3.34	1.32	1.90	2.51
Multimodal	$+y$	0.077	133475	0.83	82751	7.18	1.38	2.30	3.17
Multimodal	$+y+e$	0.074	133475	0.83	82002	7.85	1.31	2.44	3.19
Multimodal	$+y$-e	0.080	133475	0.83	82870	6.56	1.43	2.30	3.28
Multimodal	$-y$	0.074	133475	0.83	101861	6.22	1.57	2.18	3.42
Multimodal	$-y+e$	0.071	133475	0.83	100505	5.39	1.49	2.07	**3.08**
Multimodal	$-y$-e	0.071	133475	0.83	101806	6.91	1.35	2.29	3.09

T_0 fundamental period, m_0 mass, Γ participation factor, f_y yield base shear, μ_0 ductility capacity, OSR overstrength ratio, q_0 force reduction factor, q behavior factor.

Table A3
Results obtained in the case of unimodal load distribution.

Load distribution	Load combination	T_0 [s]	m_0[kg]	Γ	f_y [daN]	μ_0	OSR	q_0	q
Unimodal	$+x$	0.145	137535	1.02	50595	3.97	1.25	2.02	2.52
Unimodal	$+x+e$	0.140	137535	1.02	50591	4.18	1.21	2.07	**2.51**
Unimodal	$+x$-e	0.149	137535	1.02	50405	4.36	1.25	2.13	2.67
Unimodal	$-x$	0.176	137535	1.02	38578	3.85	1.45	2.12	3.08
Unimodal	$-x+e$	0.177	137535	1.02	39660	3.64	1.55	2.04	3.17
Unimodal	$-x$-e	0.177	137535	1.02	37901	3.90	1.43	2.14	3.06
Unimodal	$+y$	0.137	133475	0.83	48814	3.25	1.69	1.74	2.93
Unimodal	$+y+e$	0.140	133475	0.83	47041	3.24	1.64	1.74	2.85
Unimodal	$+y$-e	0.138	133475	0.83	50521	3.17	1.77	1.70	3.01
Unimodal	$-y$	0.096	133475	0.83	81022	4.02	1.70	1.81	3.07
Unimodal	$-y+e$	0.097	133475	0.83	79357	3.73	1.61	1.73	**2.79**
Unimodal	$-y$-e	0.092	133475	0.83	82914	4.60	1.83	1.93	3.52

Table A4
Results obtained in the case of triangular load distribution.

Load distribution	Load combination	T_0 [s]	m_0[kg]	Γ	f_y [daN]	μ_0	OSR	q_0	q
Triangular	$+x$	0.135	137535	1.02	52755	6.17	1.92	2.62	5.03
Triangular	$+x+e$	0.130	137535	1.02	53043	7.54	2.01	2.89	5.80
Triangular	$+x$-e	0.141	137535	1.02	52932	5.21	1.86	2.38	4.43
Triangular	$-x$	0.160	137535	1.02	39619	5.30	1.71	2.49	4.26
Triangular	$-x+e$	0.149	137535	1.02	39387	4.84	1.68	2.29	3.84
Triangular	$-x$-e	0.172	137535	1.02	38966	4.22	1.73	2.20	**3.81**
Triangular	$+y$	0.101	133475	0.83	74385	4.72	1.71	1.99	3.39
Triangular	$+y+e$	0.099	133475	0.83	79426	4.48	1.68	1.94	**3.26**
Triangular	$+y$-e	0.095	133475	0.83	75626	5.62	1.87	2.21	4.12
Triangular	$-y$	0.086	133475	0.83	102934	5.73	2.24	2.13	4.78
Triangular	$-y+e$	0.090	133475	0.83	101153	4.38	2.03	1.85	3.76
Triangular	$-y$-e	0.085	133475	0.83	104251	6.61	2.40	2.32	5.56

T_0 fundamental period, m_0 mass, Γ participation factor, f_y yield base shear, μ_0 ductility capacity, OSR overstrength ratio, q_0 force reduction factor, q behavior factor.

References

[1] D. Addessi, E. Sacco, Nonlinear analysis of masonry panels using a kinematic enriched plane state formulation, Int. J. Solids Struct. 90 (2016) 194–214.
[2] S.S. Ali, A.W. Page, Finite element model for masonry subjected to concentrated loads, J. Struct. Eng. 114 (8) (1988) 1761–1784.
[3] Augenti N., Parisi F., 2019. Teoria e tecnica delle strutture in muratura. Analisi e progettazione (In Italian). Hoepli, Milano, Italy.
[4] Benedetti D., 2004. Costruzioni in muratura: duttilità, norme ed esperienze (in Italian). Ing. Sismica, 3, 5–18.
[5] Blume J.A., 1977. Allowable stresses and earthquake performance. Proceedings of the 6th World Conference on Earthquake Engineering, New Delhi, India, 165–174.

[6] R. Brincker, L. Zhang, P. Andersen, Modal identification of output-only systems using frequency domain decomposition, Smart Mater. Struct. 10 (3) (2001) 441–445.
[7] R. Brincker, C. Ventura, Introduction to Operational Modal Analysis, Wiley, United Kingdom, 2015.
[8] P. Cacciola, P. Colajanni, G. Muscolino, Combination of modal responses consistent with seismic input representation, J. Struct. Eng. 130 (1) (2004) 47–55.
[9] P. Cacciola, L. D'Amico, I. Zentner, New insights in the analysis of the structural response to response-spectrum-compatible accelerograms, Eng. Struct. 78 (2014) 3–16.
[10] I. Capanna, R. Cirella, A. Aloisio, F. Di Fabio, M. Fragiacomo, Operational modal analysis and non-linear dynamic simulations of a prototype low-rise masonry building, Buildings 11 (10) (2021) 1–22, 471.
[11] A. Chopra, R. Goel, A Modal Pushover Analysis Procedure to Estimate Seismic Demands for Buildings: Theory and Preliminary Evaluation. PEER Report 2001/03, Pacific Earthquake Engineering Research Center, University of California, Berkeley, 2001.
[12] A.K. Chopra, Dynamics of structures: theory and applications to earthquake engineering, Prentice-Hall, Upper Saddle River, New Jersey, 2001.
[13] Cole H.A., 1973. On-line failure detection and damping measurement of aerospace structures by random decrement signatures, NASA CR-2205.
[14] A.M. D'Altri, F. Cannizzaro, M. Petracca, D.A. Talledo, Nonlinear modelling of the seismic response of masonry structures: calibration strategies, Bull. Earthq. Eng. 20 (5) (2021) 1999–2043.
[15] Decree of October 22, 2010. Arrêté du 22 octobre 2010 relatif à la classification et aux règles de construction parasismique applicables aux bâtiments de la classe dite " à risque normal ", version en vigueur au 19 octobre 2021. Official Journal of the French Republic (in French).
[16] Der Kiureghian A., 1979. On response of structures to stationary excitation. Report No. UCB/EERC-79/32, Earthquake Engineering Research Center, University of California, Berkeley, California.
[17] M. Diaferio, D. Foti, N.I. Giannoccaro, S. Ivorra, Optimal model through identified frequencies of a masonry building structure with wooden floors, Int. J. Mech. 8 (2014) 282–288.
[18] EN 1998–1, 2004. Eurocode 8: Design of Structures for earthquake resistance - Part 1: General rules, seismic actions and rules for buildings. CEN, Brussels, Belgium.
[19] EN 1996–1-1, 2005. Eurocode 6- Design of masonry structures - Part 1–1: General rules for reinforced and unreinforced masonry structures. CEN, Brussels, Belgium.
[20] EN 1998–3, 2005. Eurocode 8: Design of Structures for earthquake resistance - Part 3: Assessment and retrofitting of buildings. CEN, Brussels, Belgium.
[21] D.J. Ewins. Modal testing: theory and practice, 2nd ed., Research studies press Ltd, Hertfordshire, England, 2000.
[22] P. Fajfar, Capacity spectrum method based on inelastic demand spectra, Earthq. Eng. Struct. Dyn. 28 (9) (1999) 979–993.
[23] P. Fajfar, A nonlinear analysis method for performance-based seismic design, Earthq. Spectra 16 (3) (2000) 573–592.
[24] G.W. Fernandez Lorenzo, M.P. Santisi d'Avila, A. Deschamps, E. Bertrand, E.D. Mercerat, L. Foundotos, F. Courboulex, Numerical and empirical simulation of linear elastic seismic response of a building: the case of Nice Prefecture, Earthq. Spectra 34 (2018) 169–196.
[25] Galasco A., Lagomarsino S., Penna A., 2006. On the use of pushover analysis for existing masonry buildings. Proceedings of the 1st European Conference on Earthquake Engineering and Seismology, Geneva, Switzerland, Paper No. 1080.
[26] Gambarotta L., Lagomarsino S., 1996. On dynamic response of masonry panels (in Italian). Proceedings of the National Conference on Masonry Mechanics between theory and practice, Messina, Italy.
[27] C. Gentile, A. Saisi, Ambient vibration testing of historic masonry towers for structural identification and damage assessment, Constr. Build. Mater. 21 (2007) 1311–1321.
[28] G. Guerrini, F. Graziotti, A. Penna, G. Magenes, Improved evaluation of inelastic displacement demands for short-period masonry structures, Earthq. Eng. Struct. Dyn. 46 (9) (2017) 1411–1430.
[29] T.J.R. Hughes, The finite element method, linear static and dynamic finite element analysis, Prentice-Hall, 1987.
[30] Jennings P.C., Housner G.W., Tsai N.C., 1969. Simulated earthquake motions for design purpose. Proceedings of the 4th World Conference on Earth. Eng, Santiago, A-1, 145–160.
[31] H. Krawinkler, G.D.P.K. Seneviratna, Pros and cons of a pushover analysis of seismic performance evaluation, Eng. Struct. 20 (4–6) (1998) 452–464.
[32] S. Lagomarsino, A. Penna, A. Galasco, S. Cattari, TREMURI program: an equivalent frame model for the nonlinear seismic analysis of masonry buildings, Eng. Struct. 56 (2013) 1787–1799.
[33] H.R. Lotfi, P.B. Shing, Interface model applied to fracture of masonry structures, J. Struct. Eng. 120 (1) (1994) 63–80.
[34] P.B. Lourenço, J.G. Rots, J. Blaauwendraad, Two approaches for the analysis of masonry structures: Micro and macro-modeling, Heron 40 (4) (1995) 313–340.
[35] P.B. Lourenço, J.G. Rots, Multisurface interface model for analysis of masonry structures, J. Eng. Mech. 123 (7) (1997) 660–668.
[36] G. Magenes, G.M. Calvi, In-plane seismic response of brick masonry walls, Earthq. Eng. Struct. Dyn. 26 (11) (1997) 1091–1112.
[37] Magenes G., Della Fontana A., 1998. Simplified non-linear seismic analysis of masonry buildings. Proceedings of the 5th International Masonry Conference, London, 190 –195.
[38] Magenes G., 2000. A method for pushover analysis in seismic assessment of masonry buildings. Proceedings of the 12th World Conference on Earthquake Engineering, Auckland, New Zealand.
[39] E. Miranda, V.V.B. Bertero, Evaluation of strength reduction factors for earthquake-resistant design, Earthq. Spectra 10 (2) (1994) 357–379.
[40] A. Montabert, E.D. Mercerat, H. Lyon-Caen, M. Lancieri, Highlighting the impact of the construction history of a cultural heritage building through a vibration-based finite element model updated by particle swarm algorithm, Int. J. Archit. Herit. (2023).
[41] P. Morandi, C. Butenweg, K. Breis, K. Beyer, G. Magenes, Latest findings on the behaviour factor q for the seismic design of URM buildings, Bull. Earthq. Eng. 20 (2022) 5797–5848.
[42] Nassar A.A., Krawinkler H., 1991. Seismic demands for SDOF and MDOF systems, Report No. 95, The J. Blume Earthquake Engineering Center, Stanford University, Palo Alto.
[43] Newmark N.M., Hall W.J., 1973. Seismic design criteria for nuclear reactor facilities. Report No. 46, Building Practices for Disaster Mitigation, National Bureau of Standards, US Department of Commerce, 209 –236.
[44] Newmark N.M., Hall W.J., 1982. Earthquake spectra and design. Berkeley, CA: Earthquake Engineering Research Institute.
[45] NTC2018, 2018. Decreto Ministeriale 17 Gennaio 2018: Aggiornamento delle "Norme tecniche per le costruzioni" (in Italian), S.O. No. 8 alla G.U. del 20 Febbraio 2018, No. 42, Ministero delle Infrastrutture e dei Trasporti, Rome, Italy.
[46] F. Parisi, N. Augenti, Seismic capacity of irregular unreinforced masonry walls with openings, Earthq. Eng. Struct. Dyn. 42 (1) (2013) 101–121.
[47] M. Pastor, M. Binda, T. Harčarik, Modal Assurance Criterion, Procedia Eng. 48 (2012) 543–548.
[48] A. Penna, S. Lagomarsino, A. Galasco, A nonlinear macroelement model for the seismic analysis of masonry buildings, Earthq. Eng. Struct. Dyn. 43 (2) (2013) 159–179.
[49] J.R. Riddington, M.Z. Ghazali, Hypothesis for shear failure in masonry joints, Proc. Inst. Civ. Eng., Part 2 89 (1) (1990) 89–102.
[50] P. Roca, C. Molins, A.R. Mari, Strength capacity of masonry wall structures by the equivalent frame method, J. Struct. Eng. 131 (10) (2005) 1601–1610.
[51] J.G. Rots, Numerical simulation of cracking in structural masonry, Heron 36 (2) (1991) 49–63.
[52] M. Shinozuka, C.M. Jan, Digital simulation of random processes and its application, J. Sound Vib. 25 (1) (1972) 111–128.
[53] M. Tomaževič, Earthquake-resistant design of masonry buildings, Imperial College Press, London, U.K, 1999.
[54] Tomaževič M., Bosiljkov V., Weiss P., 2004. Structural behaviour factor for masonry structures, Proceedings of the 13th World Conference on Earthquake Engineering, Vancouver B.C., Canada, paper no. 2642.
[55] C.M. Uang, Establishing R (or Rw) and Cd factors for building seismic provisions, J. Struct. Eng. 117 (1) (1991) 19–28.
[56] E.H. Vanmarcke, Properties of spectral moments with applications to random vibration, J. Eng. Mech. 98 (2) (1972) 425–446.

[57] Vanmarcke E.H., Gasparini D.A., 1977. Simulated earthquake ground motions. Proceedings of the 4th International Conference on Structural Mechanics in Reactor Technology, San Francisco, USA, K 1/9.
[58] Veletsos A.S., Newmark N.M., 1960. Effect of inelastic behavior on the response of simple systems to earthquake motions. Proceedings of the 2nd World Conference on Earthquake Engineering, Japan, 895–912.
[59] T. Vidiç, P. Fajfar, M. Fischinger, Consistent inelastic design spectra: Strength and displacement, Earthq. Eng. Struct. Dyn. 23 (5) (1994) 507–521.